PNAS RESEARCH ARTICLE | PHYSICS OPEN ACCESS

Nuclear magnetic resonance diffraction with subangstrom precision

Holger Haas[a,b,1,2], Sahand Tabatabaei[a,b,1], William Rose[c], Pardis Sahafi[a,b], Michèle Piscitelli[a,b,3], Andrew Jordan[a,b], Pritam Priyadarsi[a,b], Namanish Singh[a,b], Ben Yager[a,b,4], Philip J. Poole[d], Dan Dalacu[d], and Raffi Budakian[a,b,5]

Edited by J. C. Davis, University of Oxford, Oxford, United Kingdom; received May 28, 2022; accepted August 31, 2022

We have combined ultrasensitive force-based spin detection with high-fidelity spin control to achieve NMR diffraction (NMRd) measurement of ∼2 million ^{31}P spins in a $(50\ \mathrm{nm})^3$ volume of an indium-phosphide (InP) nanowire. NMRd is a technique originally proposed for studying the structure of periodic arrangements of spins, with complete access to the spectroscopic capabilities of NMR. We describe two experiments that realize NMRd detection with subangstrom precision. In the first experiment, we encode a nanometer-scale spatial modulation of the z-axis magnetization of ^{31}P spins and detect the period and position of the modulation with a precision of <0.8 Å. In the second experiment, we demonstrate an interferometric technique, utilizing NMRd, to detect an angstrom-scale displacement of the InP sample with a precision of 0.07 Å. The diffraction-based techniques developed in this work extend the Fourier-encoding capabilities of NMR to the angstrom scale and demonstrate the potential of NMRd as a tool for probing the structure and dynamics of nanocrystalline materials.

magnetic resonance | scattering | MRI

Scattering techniques that employ coherent sources, such as X-rays, neutrons, and electrons, are universal tools in many branches of natural science for exploring the structure of matter. In crystalline materials, these approaches provide a direct and efficient means of characterizing the periodicity of charge and magnetic order. MRI, like other scattering approaches, is a reciprocal space technique, in which the measured signal is proportional to the Fourier transform of the spin density. This similarity between MRI and scattering was recognized very early in the development of MRI and led Mansfield and Grannell in 1973 to propose NMR "diffraction" (NMRd) as a method for determining the lattice structure of crystalline solids (1–3), taking advantage of the chemical specificity of NMR.

The main challenge to achieving atomic-scale NMRd lies in the difficulty of generating a sufficiently large wavenumber k, capable of encoding a relative phase difference as large as 2π between adjacent spins on a lattice, separated by angstrom-scale distances. For example, the largest encoding wavenumbers achieved in clinical high-resolution MRI scanners are of order $k/(2\pi) \sim 10^4\ \mathrm{m}^{-1}$, more than a factor of 10^5 smaller than what is needed to measure typical atomic spacings in condensed-matter systems (4). Consequently, while MRI has become a transformative technique in medical science, earning Sir Peter Mansfield and Paul Lauterbur the Nobel Prize in Physiology and Medicine, the original vision of NMRd as a method for exploring material structure has not yet been realized.

The realization of atomic-scale NMRd would be a powerful tool for characterizing periodic nuclear spin structures, combining the spectroscopic capabilities of NMR with spatial encoding at condensed matter's fundamental length scale. NMRd is a phase-sensitive technique that permits real-space reconstruction of the spin density, without the loss of phase information common to scattering techniques, such as X-rays, that measure the scattered-field intensity (5). Being nondestructive and particularly sensitive to hydrogen, NMRd could be of great importance in the study of ordered biological systems, such as protein nanocrystals that are of great interest in structural biology (6, 7). Furthermore, the combination of scattering with NMR's rich repertoire of spectroscopic tools opens additional avenues for spatially resolved studies of nuclear-spin Hamiltonians (e.g., chemical shifts or spin–spin interactions), which are currently achieved only through increasingly complex and indirect methods (8). Finally, NMRd could be used to study quantum many-body dynamics on the atomic scale. NMR scattering experiments have previously been used in the direct measurement of spin diffusion in CaF_2 on the micrometer scale (9). Experiments on many-body dynamics have also been conducted in engineered quantum simulators, such as ultracold atoms (10–12), trapped ions (13–15), superconducting circuits (16–18), and quantum dots (19). However, these measurements have thus far been limited to small-scale quantum systems that are at most hundreds of qubits. Angstrom-scale NMRd measurements would permit studying the dynamics of complex large-scale spin

Significance

Prior to the development of MRI, Mansfield and Grannell proposed NMR diffraction (NMRd) as a method to investigate the structure of crystalline materials. When realized on the atomic scale, NMRd would be a powerful tool to study the structure of materials, utilizing the spectroscopic capabilities of NMR. The main challenge to achieving this goal lies in the ability to encode large relative phase differences between neighboring nuclear spins on the atomic scale. Utilizing key advances in nanoMRI technology, we demonstrate the ability to encode and detect angstrom-scale modulation of approximately 2 million ^{31}P spins in an indium-phosphide (InP) nanowire with subangstrom precision. The work represents a significant step toward the realization of atomic-scale NMRd.

Author contributions: H.H., S.T., W.R., and R.B. designed research; H.H., S.T., W.R., and R.B. performed research; P.S., M.P., A.J., B.Y., P.J.P., and D.D. contributed new reagents/analytic tools; H.H., S.T., W.R., P.P., N.S., and R.B. analyzed data; H.H., S.T., and R.B. wrote the paper; and R.B. supervised the project.

The authors declare no competing interest.

This article is a PNAS Direct Submission.

[1]H.H. and S.T. contributed equally to this work.

[2]Present address: IBM Quantum, IBM T. J. Watson Research Center, Yorktown Heights, NY 10598.

[3]Present address: Clarendon Laboratory, Department of Physics, University of Oxford, Oxford OX1 3PU, United Kingdom.

[4]Present address: Oxford Instruments NanoScience, Tubney Woods, Abingdon, Oxfordshire OX13 5QX, United Kingdom.

[5]To whom correspondence may be addressed. Email: rbudakian@uwaterloo.ca.

This article contains supporting information online at https://www.pnas.org/lookup/suppl/doi:10.1073/pnas.2209213119/-/DCSupplemental.

Published September 26, 2022.

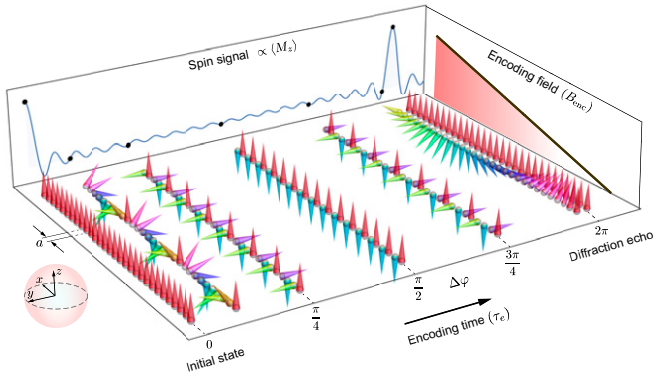

Fig. 1. Time evolution of a one-dimensional periodic lattice of spins, starting from a uniform z state at $\tau_e = 0$, under a linearly varying external field along the lattice. Each time slice represents an ensemble nuclear spin state with a well-defined **k** vector. The x, y, z coordinate axes on the left mark the Bloch sphere directions for the spins represented by the cones. For $\tau_e > 0$, the spins dephase and the expectation value of the z-axis magnetization $\langle M_z \rangle$ drops to zero. Once the spins on adjacent lattice sites complete a full rotation ($\Delta\varphi = 2\pi$), the spins rephase and a diffraction echo in $\langle M_z \rangle$ appears.

networks in condensed-matter systems on length scales as short as the lattice spacing.

Over the past two decades the principal technologies needed to encode nuclear spin states with wavenumbers of order 1 Å^{-1} have been developed in the context of force-detected nanoMRI (20–26). In this work, we report two experiments that utilize key advances in nanoMRI technology—namely the ability to generate large time-dependent magnetic-field gradients and the ability to detect and coherently control nanoscale ensembles of nuclear spins (27–31)—to generate encoding wavenumbers as large as $k/(2\pi) \sim 0.48\ \text{Å}^{-1}$.

Our first experiment demonstrates the use of spatial spin-state modulation that encodes position information the way it was envisioned in the initial NMRd proposal. Phase-sensitive NMRd detection enables us to determine the position and period of a "diffraction grating" with a precision of <0.8 Å. The diffraction grating itself is a z-axis ^{31}P spin magnetization modulation, the mean period of which is 4.5 nm in our $(50\ \text{nm})^3$ detection volume. Our second experiment utilizes spatially modulated spin phase in an alternative way—as a label for the physical displacement of the spins. Our interferometric technique detects an angstrom-scale displacement of the indium-phosphide (InP) sample with a precision of 0.07 Å.

Principles

NMRd Concept. To illustrate the basic concept of NMRd as envisioned in ref. 1, we consider a one-dimensional spin density having a spatially periodic modulation—such as a linear spin chain with spacing a as shown in Fig. 1—that evolves in a uniform field gradient $G_x = \partial B/\partial x$ for a time τ_e. The wavevector corresponding to the helical winding encoded in the spins is $k_x = \gamma\, G_x\, \tau_e$, where γ is the spin gyromagnetic ratio. At particular encoding times $\tau_{\text{echo}} = 2\pi l/(\gamma\, G_x\, a)$, corresponding to $k_x a = 2\pi l$, the relative phase between neighboring spins becomes $\Delta\varphi = 2\pi l$, $l \in \{1, 2, 3, \dots\}$ and a "diffraction echo" (DE) is observed. At the peak of the echo, the signal from each spin adds constructively, in exact analogy to the diffraction peak observed in a scattering experiment. The lattice constant is determined from the location of the DE peak and the shape of the sample from the Fourier transform of the DE envelope. Because the encoding wavevector is spin selective, the structure factor corresponding to each NMR-active nucleus can be determined separately. The NMRd concept illustrated in Fig. 1 can be readily generalized to three dimensions, with $\mathbf{k} = \gamma \mathbf{G} \tau_e$ and $\mathbf{G} = \boldsymbol{\nabla} B$, where B represents the magnitude of either the static or the radio frequency (RF) field at the Larmor frequency, used for phase encoding. The diffraction condition in three dimensions corresponds to $\mathbf{k} \cdot \mathbf{a}_j = 2\pi l$, where $\mathbf{a}_j$ are the primitive vectors of the lattice.

Being particularly sensitive to hydrogen atoms, NMRd could enable structural characterization of nanocrystalline organic solids via NMR. For example, a lattice of ^{1}H spins with $a = 3$ Å evolving under a uniform field gradient of 10^5 T/m would produce a DE at $\tau_e = 780$ µs. While the dephasing times in most organic solids are much shorter, typically of order $T_2 \sim 20$ µs, dynamical decoupling NMR pulse sequences, such as the symmetric magic echo sequence (32), can be used to extend the coherence time into the millisecond range, while allowing for encoding with both static and resonant RF field gradient pulses. Importantly, although the concept of NMRd was first envisioned as a technique to study crystal structures, it can be applied more broadly to probe any spatially periodic spin-state modulation, e.g., a periodic modulation of the z-axis magnetization, that can be refocused by the evolution under the field gradient. The magnetization modulation could, for example, also arise from evolution under internal spin Hamiltonians such as spectroscopic shifts or spin–spin interactions, both of which could be studied on atomic length scales.

Experimental Setup. The experimental setup, shown in Fig. 2*A*, is similar to the one used in our previous nanoMRI work (24). Force-detected magnetic resonance measurements were performed using a silicon nanowire (SiNW) mechanical resonator, which served as the mechanical sensor to detect the force exerted on ^{31}P spins in an InP nanowire (InPNW) placed in a magnetic-field gradient. The InPNW sample was attached to the SiNW resonator with the axes of the two nanowires aligned parallel to each other. To apply various control signals to the SiNW, we glued the SiNW chip to a millimeter-size piezo electric transducer (PT). To increase the measurement bandwidth of the resonator, a feedback signal was applied to the PT (33). For details of the SiNW and InPNW growth and attachment, see *Materials and Methods* and *SI Appendix*.

NMR measurements were performed by applying a static field of $B_0 = 3$ T parallel to the the InPNW axis. At this field, the Larmor frequency of the ^{31}P spins is $\omega_0/(2\pi) = 51.7$ MHz. The time-varying magnetic fields and magnetic-field gradients used for spin measurements were generated using a current-focusing field gradient source (CFFGS) (*Materials and Methods*). All measurements were carried out with the tip of the InPNW placed at the center of the CFFGS and positioned ∼50 nm above the surface.

The transverse field in the rotating frame $B_1(\mathbf{r}) = \sqrt{B_x^2(\mathbf{r}) + B_y^2(\mathbf{r})}/2$ used for NMR was produced by driving the CFFGS with 70 mA-peak currents at ω_0, where $B_x(\mathbf{r})$, $B_y(\mathbf{r})$, and $B_z(\mathbf{r})$ are the components of the magnetic field at position $\mathbf{r}$. Correspondingly, each spin has a Rabi frequency $u(\mathbf{r}) = \gamma B_1(\mathbf{r})/(2\pi)$, where $\gamma/(2\pi) = 17.235$ MHz/T is the ^{31}P gyromagnetic ratio. Further details regarding the field profile produced by the CFFGS are provided in *SI Appendix*.

Results

Nanometer-Scale NMRd Measurements. To observe a focused diffraction echo—i.e., one in which the spectral weight of the echo is localized within a narrow range of encoding times—the spin-state modulation must be a periodic function of the encoding-field coordinate; e.g., for a spin density with a spatially

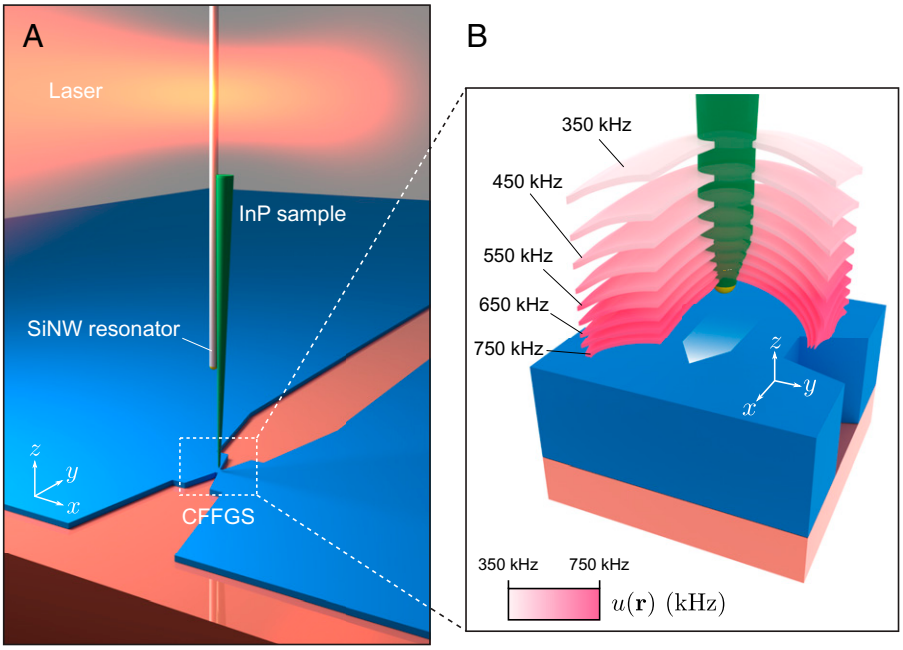

Fig. 2. (*A*) Schematic of the experimental setup, including the SiNW force sensor, the CFFGS, and the InP spin sample. (*B*) Simulated contours of constant Rabi frequency $u(\mathbf{r})$. The contours within the sample are nearly parallel to the *xy* plane and vary primarily in the *z* direction.

periodic modulation, the encoding-field profile must vary linearly in space as in Fig. 1. As a demonstration of nanometer-scale NMRd, we utilize the B_1 gradient to 1) create a diffraction grating by periodically inverting the z-axis magnetization of the ^{31}P spins within the measured volume of the InP tip (Fig. 3) and 2) generate the encoding wavevector for the NMRd measurements. In so doing, we ensure that the spin modulation is a periodic function of the encoding field.

We detect the statistical spin fluctuations in an ensemble of approximately 2×10^6 ^{31}P spins within the conical region of the InP sample indicated in Fig. 3 *A*, *Inset*, using the modulated alternating gradients generated with currents (MAGGIC) spin detection protocol described in *SI Appendix* and ref. 24. The measured spin signal is proportional to the quantity $s \propto \int d^3r\ n(\mathbf{r}) G_R^2(\mathbf{r}) \chi(u(\mathbf{r})) \mathrm{Tr}[\sigma_z \varrho_f(\mathbf{r})]$, where $n(\mathbf{r})$ is the spin density, $G_R(\mathbf{r}) = \partial B_z(\mathbf{r})/\partial y$ is the readout gradient applied in

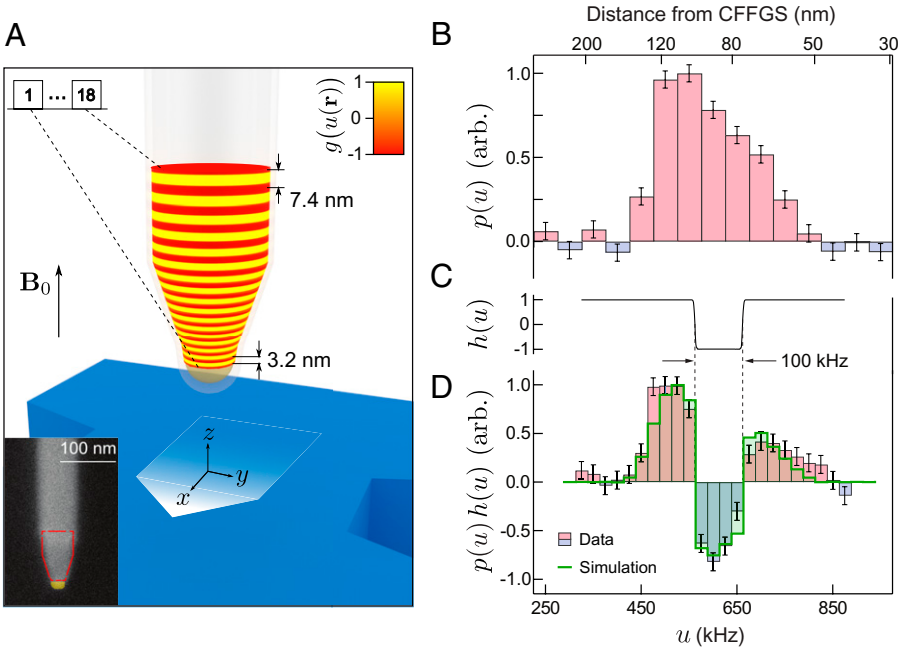

Fig. 3. (*A*) Spatial configuration of the InP spin sample brought 50 nm above the surface of the CFFGS device. The CFFGS surface lies perpendicular to the static external magnetic field $B_0\,\hat{\mathbf{z}}$. The 18 regions indicated in red represent the regions inverted by the band-inversion pulses within $g(u)$. (*Inset*) Scanning electron microscope (SEM) image of a representative InPNW. The measured volume of the sample is indicated by the outlined region. (*B*) Measured weighted Rabi-frequency distribution $p(u)$ of the ^{31}P spins in the detection volume indicated by the outlined region in *A*, *Inset*. The data were obtained by sampling 20 points in the frequency range $0 \leq u \leq 1$ MHz. The upper horizontal axis indicates the *z* coordinate corresponding to the particular *u* value on the InPNW axis at the center of the CFFGS ($x = y = 0$). (*C*) Calculated inversion profile $h(u)$ for the 100-kHz-wide band-inversion pulse, targeting spins in the Rabi frequency range 562.5 kHz $\leq u \leq$ 662.5 kHz. (*D*) Spin signal measured after applying the band-inversion profile shown in *C*. The data were obtained by sampling 23 points in the frequency range 325 kHz $\leq u \leq$ 875 kHz. The solid green line indicates the expected distribution calculated using the measured $p(u)$ in *B* and the calculated $h(u)$ in *C*.

the MAGGIC protocol that couples the z-axis magnetic moment of a spin at position $\mathbf{r}$ to the resonant mechanical motion of the SiNW, and $\chi(u)$ is a Rabi-frequency–dependent filter function used to control the detection volume (*SI Appendix*). Here, $\varrho_f(\mathbf{r})$ is the traceless part of the density matrix of the spin at position $\mathbf{r}$ at the end of the NMR control sequence, $\mathrm{Tr}[\sigma_z \varrho_f(\mathbf{r})]$ is proportional to the expectation value of the z-axis component of the magnetic moment of the spin, and $(\sigma_x, \sigma_y, \sigma_z)$ are the Pauli spin operators.

For the case where the NMR control sequence is only selective in Rabi frequency, ϱ_f is only a function of u, such that $s \propto \int_0^\infty du\ p(u)\mathrm{Tr}[\sigma_z \varrho_f(u)]$, where $p(u)$ is the weighted Rabi frequency distribution, determined by the sample geometry, the readout gradient $G_R(\mathbf{r})$, and the filter function $\chi(u)$. For a derivation of $p(u)$ in terms of the MAGGIC protocol parameters, see *SI Appendix*. We experimentally determine $p(u)$ (Fig. 3*B*) using the Fourier-encoding method presented in ref. 24.

We encode the periodic grating $g(u)$ in the z-axis magnetization by selectively inverting sequential regions in the sample that are 10.2-kHz wide and separated by 10.2 kHz in u, as indicated in Fig. 4*A*. The physical regions targeted by the inversions are shown in Fig. 3*A*. To generate a particular $g(u)$, we implement control waveforms that invert spins within the range $(u_{\mathrm{low}}, u_{\mathrm{high}})$ with adjustable edge sharpness around u_{low} and u_{high}. To verify the performance of the inversion waveform, we implement a control sequence that inverts spins within a 100-kHz bandwidth: $562.5\ \mathrm{kHz} \le u \le 662.5\ \mathrm{kHz}$. The calculated inversion profile is shown in Fig. 3*C*. The measured spin signal after the application of the band-inversion pulse (Fig. 3*D*) agrees closely with the expected inversion profile. Further details regarding the design of the band-inversion pulses are in *SI Appendix*. We also include an animation depicting the operation of the 100-kHz-wide band-inversion pulse in Movie S2.

The NMR control sequence used to measure $g(u)$ is shown schematically in Fig. 4*C*. After encoding the grating, we apply a Larmor-frequency RF pulse for a duration τ.* The evolution of the spin, when driven with constant Rabi frequency u, is described by a unitary $U(u,\tau) = \exp(-i2\pi u\tau\sigma_x/2)$ in the frame rotating at ω_0, which yields $\varrho_f(u) = g(u)U(u,\tau)\sigma_z U^\dagger(u,\tau)/2 = g(u)[\cos(2\pi\tau u)\sigma_z - \sin(2\pi\tau u)\sigma_y]/2$. The in-phase (s_I) and quadrature (s_Q) components of the diffraction signal are

$$\begin{bmatrix} s_I(\tau) \\ s_Q(\tau) \end{bmatrix} \propto \int_0^\infty du\, p(u)g(u) \begin{bmatrix} \cos(2\pi u\tau) \\ -\sin(2\pi u\tau) \end{bmatrix}. \qquad [1]$$

To measure the quadrature part of NMRd signal, we end the measurement sequence with a numerically optimized adiabatic half-passage (AHP) pulse (34) that rotates σ_y to σ_z. It can be seen that if $g(u)$ has a single modulation period Ω, i.e., $g(u + l\Omega) = g(u)$, $l \in \mathbb{Z}$, and varies much more rapidly than the envelope of $p(u)$, then $s_I(\tau)$ and $s_Q(\tau)$ contain a series of diffraction echos separated by $1/\Omega$-long intervals. The amplitudes of these echos reflect the magnitude of the Fourier coefficients of $g(u)$, and the echo envelopes contain the Fourier transform of $p(u)$.

To demonstrate the phase, and consequently position, sensitivity of NMRd, we encode two spin magnetization gratings $g_1(u)$ and $g_2(u)$, shown in Fig. 4*A*, that differ by a 4.74-kHz translation; i.e., $g_2(u) = g_1(u + 4.74\ \mathrm{kHz})$. We refer to $g_1(u)$ and $g_2(u)$ as the grating at positions 1 and 2, respectively. The physical displacement of the grating corresponding to $\Delta u = 4.74$ kHz is $\Delta z = 0.7$ nm ($\Delta z = 1.9$ nm) at $z = 50$ nm ($z = 140$ nm). Both gratings are produced using the control sequence shown in Fig. 4*C* that comprises 18 band inversion waveforms sandwiched between two AHPs identical to the ones used to measure $s_Q(\tau)$.

Fig. 4*B* shows a plot of the expected $s_I(\tau)$ calculated using Eq. **1**, $g_1(u)$, and the measured $p(u)$ shown in Fig. 3*B*. Because the first DE at $\tau \sim 49$ μs has a significantly larger amplitude than the higher-diffraction orders, we measure the NMRd signal only for $l = 1$, for both grating positions, in the interval $39\ \mu\mathrm{s} \le \tau \le 59\ \mu\mathrm{s}$, using the NMRd measurement protocol that is shown in Fig. 4*C*. We note that for all measurements shown in Fig. 4, the maximum duration of the RF pulse used in the NMRd measurement portion of the sequence was 59 μs, which is much shorter than the transverse relaxation time $T_{2\rho} = 570$ μs measured under a continuous Larmor-frequency excitation (*SI Appendix*). Therefore, we ignore decoherence effects during the RF pulse in our analysis and simulations. The resulting data are shown in Fig. 4 *D* and *E*, which also include the unscaled calculated values for $s_I(\tau)$ and $s_Q(\tau)$. The echo envelopes for both signal quadratures are shown as the shaded regions in Fig. 4 *D* and *E*. We see that although the small shift in the grating position produces little discernible change in the echo envelope, there is a clearly visible change in the relative phase of the in-phase and quadrature measurements, demonstrating the importance of phase-sensitive detection for high-precision position measurements.

In *SI Appendix*, we construct a statistical estimator (35) to determine the periodicity Ω from the measured data. The calculation is done assuming no prior knowledge of $g(u)$, other than the fact that it is periodic in u and varies more rapidly than $p(u)$. The resulting estimates for Ω in g_1 and g_2 are $\Omega_1 = 20.30 \pm 0.14$ kHz and $\Omega_2 = 20.26 \pm 0.10$ kHz, respectively. The 0.14-kHz (0.10-kHz) error in the period of g_1 (g_2) in u space corresponds to an uncertainty of 0.2 Å (0.15 Å) in the wavelength of the grating at $z = 50$ nm and 0.6 Å (0.4 Å) at $z = 140$ nm.

In *SI Appendix*, we construct a maximum-likelihood estimator for Δu for the data in Fig. 4, which yields $\Delta u = 4.67 \pm 0.20$ kHz, in excellent agreement with the expected value of $\Delta u = 4.74$ kHz. The error in Δu corresponds to an uncertainty of 0.3 Å (0.8 Å) in the relative z-axis position of g_1 (g_2) at $z = 50$ nm ($z = 140$ nm).

We reconstruct the periodic spin modulation in spatial coordinates by calculating the real part of the complex Fourier transform $\mathrm{Re}\{\mathcal{F}^{-1}[s_I(\tau) + i\, s_Q(\tau)]\}$ using the data shown in Fig. 4 *D* and *E* for the two grating positions. In the reconstruction, we include the points around the $l = 1$ DE, as well as the points sampled near $\tau = 0$ to account for a small DC offset in the modulation envelope caused by a slight asymmetry in the magnitude of the positive- and negative-amplitude regions in $g(u)$. The time records used in the Fourier transforms are constructed to be continuous by zero-padding the unsampled regions in the interval $0 \le \tau \le 59.5$ μs (Fig. 4*B*). The data in the interval $0 \le \tau \le 3$ μs are not expected to change for the two grating positions. Therefore, this interval was measured only for position 1 and used in the reconstruction of both grating positions. We see that the position–space representations of $p(u)g_1(u)$ and $p(u)g_2(u)$, shown in Fig. 4 *F* and *G*, closely follow the calculated values.

Displacement Detection via NMR Interferometry. In the previous section, we performed phase-sensitive NMRd measurements of a nanometer-scale periodic modulation of the z-axis magnetization with subangstrom precision. In this section, we describe an interferometric detection protocol that enables us to measure a real-space displacement of the InP sample in the z direction with a precision of 0.07 Å. The protocol, shown schematically in Fig. 5*A*,

*Prior to the application of the RF pulse, we introduce a wait time $\sim 3T_2^*$, where $T_2^* = 70$ μs, to dephase any small residual transverse components in the spin magnetization that can arise from the band inversion pulses.

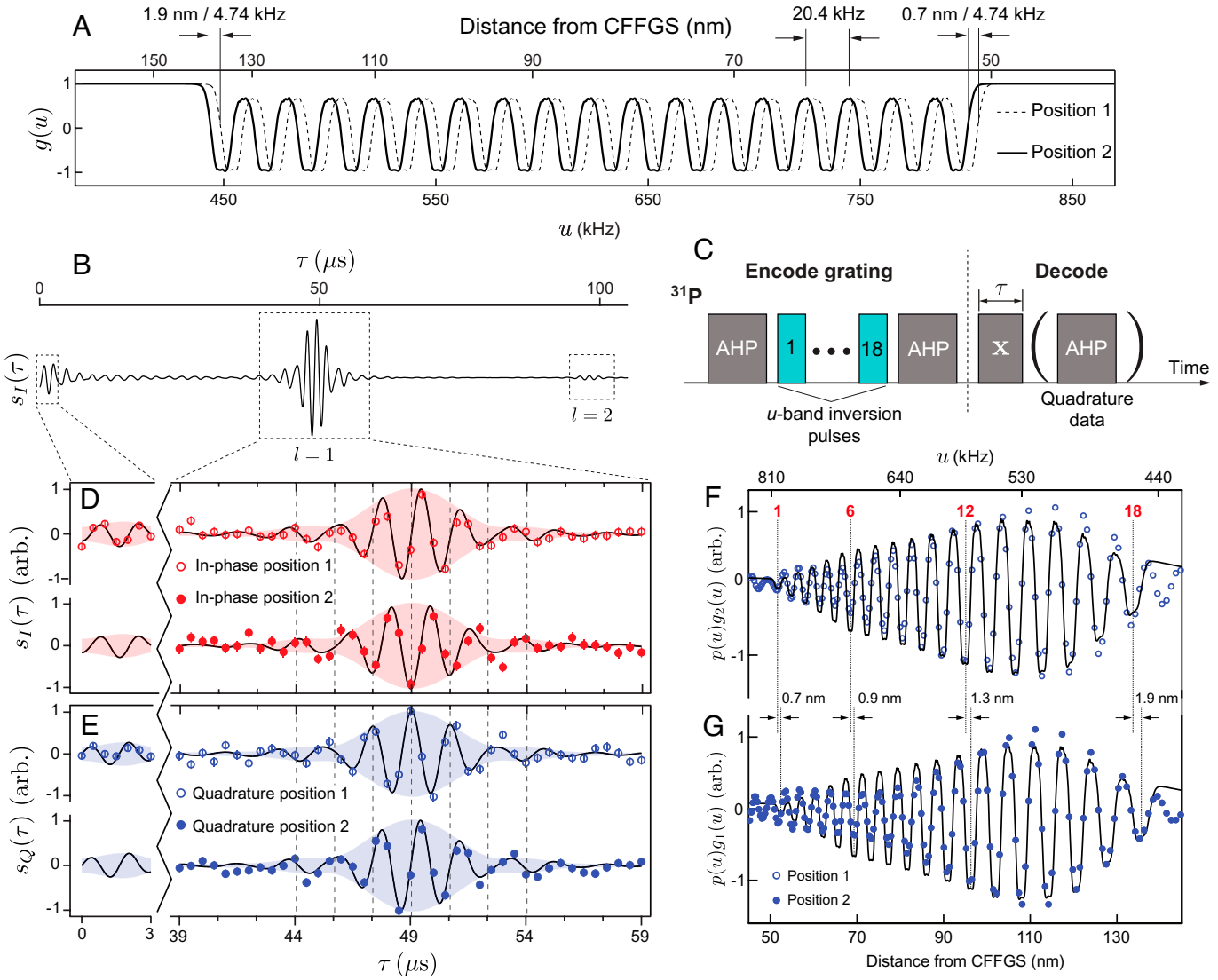

Fig. 4. NMRd data measured for the 18 × diffraction grating. (*A*) Inversion profile for the two positions (g_1 and g_2) of the periodic grating encoded with a period of 20.4 kHz. The top horizontal axis indicates the position dependence of g_1 and g_2 with respect to the CFFGS. The shift in position corresponding to $\Delta u = 4.74$ kHz is indicated for the regions of the sample that are 50 and 140 nm away from the CFFGS. (*B*) Calculated in-phase component $s_I(\tau)$ for the grating at position 1 given the simulated $g_1(u)$ profile in *A* and measured $p(u)$ shown in Fig. 3*B*. (*C*) NMR control sequence. The encoding part of the sequence generates either $g_1(u)$ or $g_2(u)$ in *A* by applying 18 consecutive inversions. The second part of the sequence performs the NMRd readout. $s_I(\tau)$ is measured by applying a resonant RF pulse (**x**) for a duration τ. An extra adiabatic half-passage pulse is applied for detecting the quadrature component $s_Q(\tau)$. (*D* and *E*) $s_I(\tau)$ and $s_Q(\tau)$ measurements for the two grating positions in *A* as a function of the effective encoding time τ. The shaded regions in *D* and *E* indicate the signal amplitude. (*F* and *G*) Coordinate–space reconstruction of the diffraction grating. Solid lines in *F* and *G* are the calculated $p(u)g_1(u)$ [$p(u)g_2(u)$] using $g_1(u)$ [$g_2(u)$] in *A* and $p(u)$ in Fig. 3*B*. The data points are the coordinate–space reconstructions of $p(u)g_1(u)$ and $p(u)g_2(u)$ by Fourier transforming the data in *D* and *E* after zero padding. The position values indicated on the lower horizontal axis are determined from the simulated field distribution produced by the CFFGS (*SI Appendix*).The dashed vertical lines are placed as a guide to indicate the spatial offset between the two grating positions. The number of the inversion slice is indicated above the vertical lines.

utilizes the symmetric magic echo (SME4) (32) NMR sequence to decouple the P-P and P-In interactions, thereby extending the coherence time of the ^{31}P spins up to 12.8 ms. In *SI Appendix*, we describe a modification to the SME4 that allows us to evolve the spins under the Rabi-frequency gradient $\partial u/\partial z = \gamma(\partial B_1/\partial z)/(2\pi)$ for a variable amount of time $\Delta\tau$ for phase encoding. By extending the spin coherence time into the millisecond range and by utilizing the large-field gradients ($\partial B_1/\partial z \sim 2 \times 10^5$ T/m) we encode a helical phase winding in the xz plane with an average wavelength as short as a few angstroms, allowing us to detect displacements of the InP sample with picometer precision.

The protocol starts by encoding a helical winding for a time τ_e. The traceless part of the density matrix for a spin at position $\mathbf{r}$ at the end of the encoding sequence is $U[u(\mathbf{r}), \tau_e]\, \sigma_z\, U^\dagger[u(\mathbf{r}), \tau_e]/2$, where $U[u(\mathbf{r}), \tau] = \exp[-i2\pi\tau\sigma_y u(\mathbf{r})/2]$. During this time, a constant voltage is applied to the PT (Fig. 5 *B*, *Inset*), which translates the InP sample with respect to the CFFGS, thereby slightly shifting the local field experienced by the ^{31}P spins during encoding. The PT is retracted to its equilibrium position by zeroing the voltage. During retraction, 2 × SME4 sequences with $\Delta\tau = 0$ are applied, contributing no gradient evolution while refocusing the homonuclear dipolar and σ_z evolution during the time that the PT returns to its equilibrium position. The duration of the 2 × SME4 sequences is 1.8 ms, which is chosen to be substantially longer than the ∼300 μs mechanical response time of the PT. In the decoding phase, the inverse unitary $U^\dagger[u(\mathbf{r}+\delta\mathbf{r}), \tau_d] = \exp[i2\pi\tau_d u(\mathbf{r}+\delta\mathbf{r})\sigma_y/2]$ is applied for a time τ_d at the new location of the InP sample, which yields $\varrho_f(\mathbf{r}+\delta\mathbf{r}) = \delta U(\mathbf{r}, \delta\mathbf{r})\sigma_z \delta U^\dagger(\mathbf{r}, \delta\mathbf{r})/2 = [\sigma_z \cos\varphi(\mathbf{r}, \delta\mathbf{r}) + \sigma_x \sin\varphi(\mathbf{r}, \delta\mathbf{r})]/2$, where $\delta U(\mathbf{r}, \delta\mathbf{r}) = \exp[-i\varphi(\mathbf{r}, \delta\mathbf{r})\sigma_y/2]$.

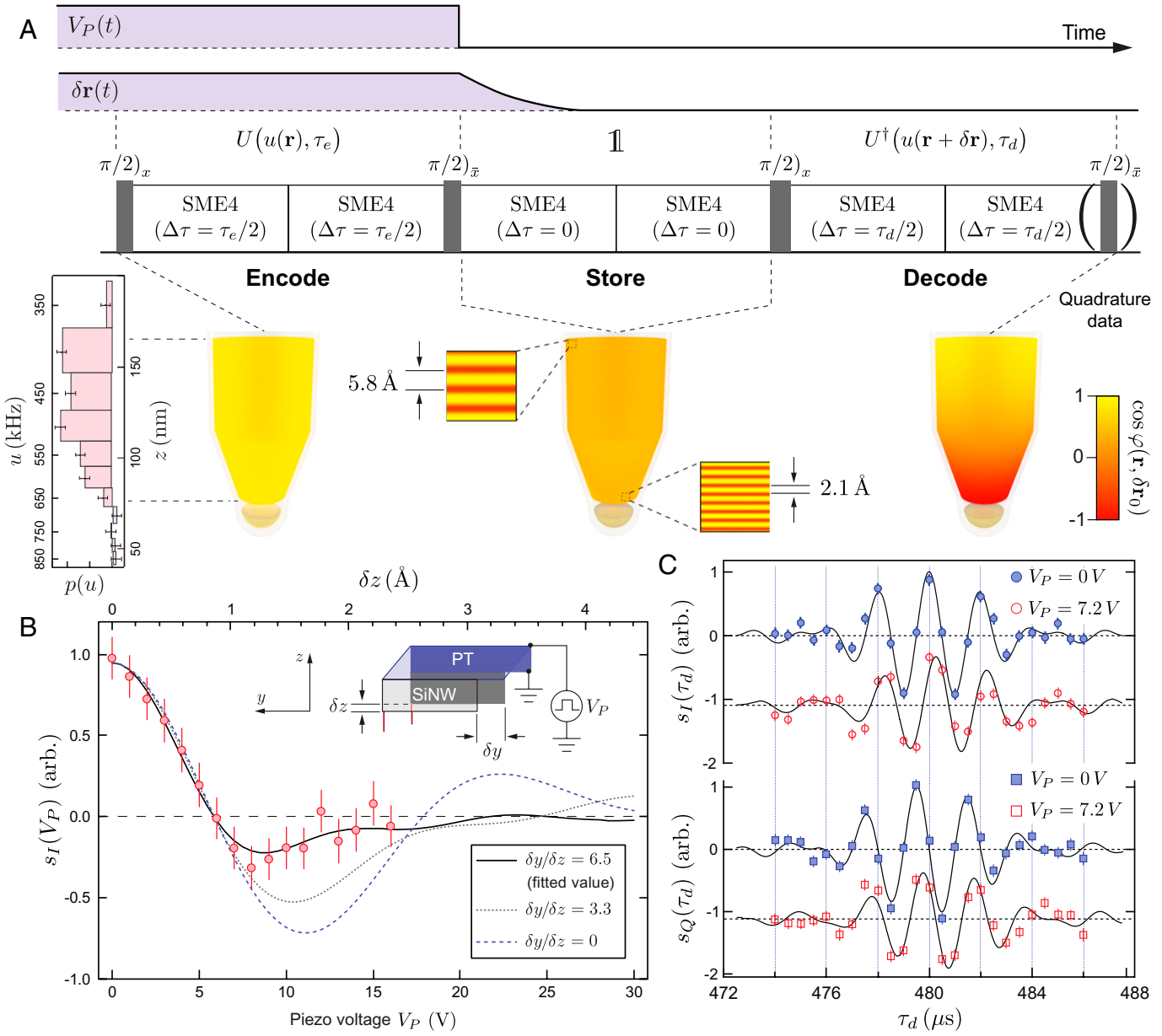

Fig. 5. (*A*) NMR control sequence used for interferometric displacement detection, as well as the voltage $V_P(t)$ applied to the PT, and the PT displacement $\delta\mathbf{r}(t)$. The unitary operations corresponding to different parts of the sequence are indicated above each block. The data presented in *B* and *C* were acquired from spins in the Rabi-frequency range 400 kHz $< u <$ 650 kHz, corresponding to the sample volume indicated by the shaded regions in *A*. The shading indicates the *z*-axis modulation $[\cos\varphi(\mathbf{r},\delta\mathbf{r}_0)]$ at different times during the measurement sequence, corresponding to $\tau_e = \tau_d = 960$ μs, and a sample displacement of $\delta\mathbf{r}_0 = 1$ Å $\hat{\mathbf{z}}$. (*B*) The data were acquired using the sequence shown in *A*, where 2 × SME4 sequences were used in the encoding portion, with each SME4 designed to encode phase for $\Delta\tau = 480$ μs. From the fit to the data, we determine the ratio $\delta y/\delta z = 6.5$. For reference, two other curves have been included that show the variation in signal amplitude for different ratios of $\delta y/\delta z$. The calculations clearly indicate that for lateral displacements of order 1 nm, a higher ratio $\delta y/\delta z$ primarily increases the decay rate with respect to V_P of the modulation envelope of the interference signal, without significantly affecting the modulation frequency; the modulation frequency, on the other hand, is primarily determined by δz. The asymmetry in the response along the *y* and *z* directions is caused by the relative magnitude of the B_1 gradients near the center of the CFFGS, for which $\partial B_1/\partial x, \partial B_1/\partial y \lesssim 0.01\partial B_1/\partial z$. (*C*) In-phase and quadrature data were acquired for $V_P = 0$ V and $V_P = 7.2$ V with a fixed encoding time of $\tau_e = 480$ μs for different decoding times. A single SME4 with $\Delta\tau = 480$ μs was used for the encoding and decoding parts of the sequence. The displacement results in a shift in the phase of both signal quadratures. From the fit to the data, we determine displacement corresponding to $V_P = 7.2$ V to be $\delta z = 0.81 \pm 0.07$ Å and $\delta y = 9.72 \pm 1.34$ Å. The value of δy determined from the fit is consistent with the value $\delta y = 1.0$ nm determined by optical interferometry (*SI Appendix*). The $V_P = 7.2$ V datasets in *C* have been offset for clarity.

The differential phase $\varphi(\mathbf{r},\delta\mathbf{r}) = 2\pi\left[u(\mathbf{r})\tau_e - u(\mathbf{r}+\delta\mathbf{r})\tau_d\right]$ results from the interference of the encoding and decoding modulations separated by $\delta\mathbf{r}$. The measured signal quadratures at the end of the sequence are

$$\begin{bmatrix} s_I(\tau_e,\tau_d,\delta\mathbf{r}) \\ s_Q(\tau_e,\tau_d,\delta\mathbf{r}) \end{bmatrix} \propto \int d^3r\; n(\mathbf{r})\, G_R^2(\mathbf{r})\chi\big(u(\mathbf{r})\big) \begin{bmatrix} \cos\varphi(\mathbf{r},\delta\mathbf{r}) \\ \sin\varphi(\mathbf{r},\delta\mathbf{r}) \end{bmatrix}. \quad [2]$$

Fig. 5*B* shows a plot of the in-phase data acquired as a function of the voltage V_P applied to the PT, using the sequence shown in Fig. 5*A*, with $\tau_d = \tau_e = 960$ μs. The modulation wavelength varies from 2.1 to 5.8 Å within the measured volume of the sample. To extract the *z* displacement from the data, we conduct a least-squares fit (36) using Eq. **2**, where we assume that $\delta\mathbf{r} \propto V_P$ and $\delta\mathbf{r} = \delta y\,\hat{\mathbf{y}} + \delta z\,\hat{\mathbf{z}}$, with the fit parameters being the PT coefficient $\delta z/V_P$ and $\delta y/\delta z$. The displacement in the *y* direction is included because the PT used for the measurements

was poled in the y direction; hence $\delta y(V_P) \gg \delta z(V_P)$. The quantity $n(\mathbf{r})G_R^2(\mathbf{r})\chi\big(u(\mathbf{r})\big)$ was calculated using our model for the sample geometry (*SI Appendix*). For details regarding the characterization of the PT, see *SI Appendix*. The resulting fit is indicated by the solid line in Fig. 5*B*, corresponding to a displacement $\delta z/V_P = 0.15 \pm 0.01$ Å/V. The PT calibration was used to derive the top horizontal axis in Fig. 5*B*.

Finally, we conduct a set of measurements in which we keep the encoding time and the voltage step applied to the PT constant and vary the decoding time. Fig. 5*C* shows the in-phase and quadrature data acquired for $V_P = 0$ V and $V_P = 7.2$ V with $\tau_e = 480$ μs. To extract the sample displacement, we fit to the data using Eq. **2**, with the fit parameters being δz and δy (solid lines in Fig. 5*C*). The fit yields a sample displacement of $\delta z = 0.81 \pm 0.07$ Å. In *SI Appendix*, we also provide an alternative fitting method, which utilizes the measured $p(u)$ instead of the geometric model of the sample. Consistent with the previous method, the fit yields $\delta z = 0.85 \pm 0.07$ Å.

Using the PT displacement calibration found in Fig. 5*B*, we would expect the displacement corresponding to $V_P = 7.2$ V to be $\delta z = 1.04 \pm 0.04$ Å. Although the calculated displacements from the two measurements are in reasonable agreement, the 20% difference in δz could be caused by systematic errors in the different methods used for determining the displacement corresponding to $V_P = 7.2$ V. In particular, to determine the PT displacement for the data in Fig. 5*B*, we needed to assume a particular functional form for the piezo characteristic $\delta\mathbf{r}(V_P)$. For the data in Fig. 5*C*, however, we find the displacement directly for one particular value of V_P, without any assumptions on $\delta\mathbf{r}(V_P)$. It is therefore possible that a small nonlinear component in $\delta\mathbf{r}(V_P)$ could be responsible for the observed difference.

For measurements that require large encoding wavevectors, such as those that would be needed for crystallographic NMRd, the mechanical stability of the sample becomes an important consideration. We provide an analysis of the effect of mechanical vibrations in *SI Appendix*, indicating sufficient mechanical stability in the reported experiments.

Discussion

In this work, we have presented two experiments that utilize the large encoding wavevectors generated in a nanoMRI setting to realize phase-sensitive NMRd measurement of ^{31}P spins with subangstrom precision. We believe these results represent substantial progress in establishing NMRd as a tool for studying material structure. With further development of gradient sources capable of applying spatially uniform encoding gradients in three dimensions (3D), NMRd could be used to study the structure of nanocrystalline materials.

Upcoming experiments focusing on NMRd crystallography will utilize a design that combines the CFFGS with four additional current-carrying paths designed to generate highly uniform 3D field gradients of order 3×10^4 T/m with a maximum variation of 0.5% in a $(100\ \text{nm})^3$ volume, suitable for crystallographic NMRd measurements. Using these gradients, ^{1}H spins separated by 3 Å, for example, would form a DE at an encoding time of 2.6 ms, which is readily achievable using dynamical-decoupling NMR sequences, such as the SME. Finally, although the concept of NMRd was first envisioned for the study of material structure, it can be applied more generally to study the dynamics of spatially periodic spin correlations. Here, we have demonstrated the ability to generate encoding wavevectors that could be used to probe spin transport on length scales as short as the lattice spacing.

Materials and Methods

SiNW Resonator. Arrays of SiNWs were grown epitaxially via the vapor–liquid–solid method from an array of Au catalyst particles patterned near the edge of a 1.5 × 1 × 0.4-mm Si(111) substrate. Growth occurred in a H_2 and HCl atmosphere using SiH_4 as the precursor. The SiNWs had a length of 20 μm and a 100-nm diameter (37). The frequency of the fundamental flexural mode of the as-grown SiNW was ∼250 kHz prior to sample attachment and had a spring constant of 0.6 mN/m. At 4 K, the quality factor of the SiNW was ∼60,000. After sample attachment, the resonance frequency of the SiNW decreased to 163 kHz; however, no significant change in the quality factor was observed. The effective quality factor of the SiNW was reduced to 700 after feedback damping through the PT.

InPNW Growth. The InPNW sample used in this work was ∼5 μm long, with an ∼50-nm diameter, grown with a Wurtzite structure. The growth was done on a SiO_2-patterned (111)B InP substrate using chemical beam epitaxy with trimethylindium (TMI) and precracked PH_3 and AsH_3 sources. The patterned substrate consisted of circular holes opened up in the SiO_2 mask using electron-beam lithography and a hydrofluoric acid wet etch into which a 5-nm-thick Au layer was deposited using a self-aligned liftoff process. To achieve precise diameter control, a two-step growth process was employed (38). First, we use growth conditions (e.g., low growth temperature, low TMI, and PH_3 fluxes) that promote incorporation of material only at the Au/InP interface (i.e., vapor–liquid–solid epitaxy) and produce defect-free wurtzite phase nanowire cores with a diameter of ∼20 nm (39). To clad the nanowire core we switch to conditions that promote material incorporation on the nanowire sidewalls (e.g., higher PH_3 flux) to controllably increase the nanowire diameter to ∼50 nm (40), see Fig. 3 *A*, *Inset*.

Sample Attachment. The InPNW sample was attached ∼3 to 4 μm away from the tip of the SiNW, with the tip of the InPNW extending ∼2 μm beyond the tip of the SiNW. Details of the attachment procedure are provided in *SI Appendix*. A video of the sample attachment is also included in Movie S1.

CFFGS Device. The CFFGS device was fabricated by electron-beam lithography and reactive ion-beam etching of a 100-nm-thick Al film deposited on a sapphire substrate. The device contained a 150-nm-wide and 50-nm-long constriction, which served to focus electrical currents to produce the magnetic fields used for spin detection and control.

Force-Detected NMR Measurements. NMR measurements were performed in high vacuum at 4 K using a custom-built force microscope with piezo nanopositioners for relative positioning of the SiNW chip, CFFGS, and the optical fiber, which was used for interferometric displacement detection of the SiNW. For details of the measurement along with a schematic of the experimental setup, see *SI Appendix*.

Data, Materials, and Software Availability. All study data are included in the article and/or *SI Appendix*.

ACKNOWLEDGMENTS. This work was undertaken due in part to funding from the US Army Research Office through Grant W911NF1610199, the Canada First Research Excellence Fund (CFREF), and the Natural Sciences and Engineering Research Council of Canada. The University of Waterloo's Quantum-Nano Fabrication and Characterization Facility (QNFCF) was used for this work. This infrastructure would not be possible without the significant contributions of Transformative Quantum Technologies (CFREF-TQT), Canada Foundation for Innovation (CFI), Industry Canada, the Ontario Ministry of Research and Innovation, and Mike and Ophelia Lazaridis. Their support is gratefully acknowledged. H.H. thanks F. Flicker, S. H. Simon, and H. S. Røising for insightful and inspiring discussions. R.B. thanks D. G. Cory and A. Cooper for useful discussions.

Author affiliations: [a]Department of Physics and Astronomy, University of Waterloo, Waterloo, ON N2L3G1, Canada; [b]Institute for Quantum Computing, University of Waterloo, Waterloo, ON N2L3G1, Canada; [c]Department of Physics, University of Illinois at Urbana–Champaign, Urbana, IL 61801; and [d]Advanced Electronics and Photonics Research Centre, National Research Council of Canada, Ottawa, ON K1A 0R6, Canada

1. P. Mansfield, P. K. Grannell, NMR 'diffraction' in solids? *J. Phys. C Solid State Phys.* **6**, L422 (1973).
2. P. Mansfield, P. K. Grannell, "Diffraction" and microscopy in solids and liquids by NMR. *Phys. Rev. B* **12**, 3618–3634 (1975).
3. P. Mansfield, Snapshot magnetic resonance imaging (Nobel lecture). *Angew. Chem. Int. Ed. Engl.* **43**, 5456–5464 (2004).
4. B. Vachha, S. Y. Huang, MRI with ultrahigh field strength and high-performance gradients: Challenges and opportunities for clinical neuroimaging at 7 T and beyond. *Eur. Radiol. Exp.* **5**, 35 (2021).
5. H. A. Hauptman, The phase problem of X-ray crystallography. *Rep. Prog. Phys.* **54**, 1427 (1991).
6. H. N. Chapman *et al.*, Femtosecond X-ray protein nanocrystallography. *Nature* **470**, 73–77 (2011).
7. M. T. B. Clabbers, J. P. Abrahams, Electron diffraction and three-dimensional crystallography for structural biology. *Crystallogr. Rev.* **24**, 176–204 (2018).
8. A. Klein *et al.*, Atomic-resolution chemical characterization of (2x)72-kDa tryptophan synthase via four- and five-dimensional ^{1}H-detected solid-state NMR. *Proc. Natl. Acad. Sci. U.S.A.* **119**, e2114690119 (2022).
9. W. Zhang, D. G. Cory, First direct measurement of the spin diffusion rate in a homogenous solid. *Phys. Rev. Lett.* **80**, 1324 (1998).
10. I. Bloch, J. Dalibard, W. Zwerger, Many-body physics with ultracold gases. *Rev. Mod. Phys.* **80**, 885–964 (2008).
11. P. N. Jepsen *et al.*, Spin transport in a tunable Heisenberg model realized with ultracold atoms. *Nature* **588**, 403–407 (2020).
12. D. Wei *et al.*, Quantum gas microscopy of Kardar-Parisi-Zhang superdiffusion. *Science* **376**, 716–720 (2022).
13. C. Monroe *et al.*, Programmable quantum simulations of spin systems with trapped ions. *Rev. Mod. Phys.* **93**, 025001 (2021).
14. Q. X. Mei *et al.*, Experimental realization of the Rabi-Hubbard model with trapped ions. *Phys. Rev. Lett.* **128**, 160504 (2022).
15. H. B. Kaplan *et al.*, Many-body dephasing in a trapped-ion quantum simulator. *Phys. Rev. Lett.* **125**, 120605 (2020).
16. K. Xu *et al.*, Emulating many-body localization with a superconducting quantum processor. *Phys. Rev. Lett.* **120**, 050507 (2018).
17. Q. Zhu *et al.*, Observation of thermalization and information scrambling in a superconducting quantum processor. *Phys. Rev. Lett.* **128**, 160502 (2022).
18. Q. Guo *et al.*, Stark many-body localization on a superconducting quantum processor. *Phys. Rev. Lett.* **127**, 240502 (2021).
19. C. J. van Diepen *et al.*, Quantum simulation of antiferromagnetic Heisenberg chain with gate-defined quantum dots. *Phys. Rev. X* **11**, 041025 (2021).
20. C. L. Degen, M. Poggio, H. J. Mamin, C. T. Rettner, D. Rugar, Nanoscale magnetic resonance imaging. *Proc. Natl. Acad. Sci. U.S.A.* **106**, 1313–1317 (2009).
21. J. M. Nichol, E. R. Hemesath, L. J. Lauhon, R. Budakian, Nanomechanical detection of nuclear magnetic resonance using a silicon nanowire oscillator. *Phys. Rev. B Condens. Matter Mater. Phys.* **85**, 054414 (2012).
22. J. M. Nichol, T. R. Naibert, E. R. Hemesath, L. J. Lauhon, R. Budakian, Nanoscale Fourier-transform magnetic resonance imaging. *Phys. Rev. X* **3**, 031016 (2013).
23. K. Arai *et al.*, Fourier magnetic imaging with nanoscale resolution and compressed sensing speed-up using electronic spins in diamond. *Nat. Nanotechnol.* **10**, 859–864 (2015).
24. W. Rose *et al.*, High-resolution nanoscale solid-state nuclear magnetic resonance spectroscopy. *Phys. Rev. X* **8**, 011030 (2018).
25. M. Barbic, Magnetic resonance diffraction using the magnetic field from a ferromagnetic sphere. *J. Appl. Phys.* **91**, 9987–9994 (2002).
26. M. Barbic, A. Scherer, Sample-detector coupling in atomic resolution magnetic resonance diffraction. *J. Appl. Phys.* **92**, 7345–7354 (2002).
27. S. H. Autler, C. H. Townes, Stark effect in rapidly varying fields. *Phys. Rev.* **100**, 703–722 (1955).
28. U. Haeberlen, J. S. Waugh, Coherent averaging effects in magnetic resonance. *Phys. Rev.* **175**, 453–467 (1968).
29. A. Tannús, M. Garwood, Improved performance of frequency-swept pulses using offset-independent adiabaticity. *J. Magn. Reson. A* **120**, 133–137 (1996).
30. M. Garwood, L. DelaBarre, The return of the frequency sweep: Designing adiabatic pulses for contemporary NMR. *J. Magn. Reson.* **153**, 155–177 (2001).
31. H. Haas, D. Puzzuoli, F. Zhang, D. G. Cory, Engineering effective Hamiltonians. *New J. Phys.* **21**, 103011 (2019).
32. G. S. Boutis, P. Cappellaro, H. Cho, C. Ramanathan, D. G. Cory, Pulse error compensating symmetric magic-echo trains. *J. Magn. Reson.* **161**, 132–137 (2003).
33. M. Poggio, C. L. Degen, H. J. Mamin, D. Rugar, Feedback cooling of a cantilever's fundamental mode below 5 mK. *Phys. Rev. Lett.* **99**, 017201 (2007).
34. S. Tabatabaei *et al.*, Numerical engineering of robust adiabatic operations. *Phys. Rev. Appl.* **15**, 044043 (2021).
35. G. Casella, R. Berger, *Statistical Inference* (Duxbury Advanced Series, Brooks/Cole Publishing Company, 1990).
36. D Sivia, J Skilling, *Data Analysis: A Bayesian Tutorial* (Oxford Science Publications [OUP Oxford], 2006).
37. P. Sahafi *et al.*, Ultralow dissipation patterned silicon nanowire arrays for scanning probe microscopy. *Nano Lett.* **20**, 218–223 (2020).
38. D. Dalacu *et al.*, Selective-area vapor-liquid-solid growth of tunable InAsP quantum dots in nanowires. *Appl. Phys. Lett.* **98**, 251101 (2011).
39. D. Dalacu *et al.*, Ultraclean emission from InAsP quantum dots in defect-free wurtzite InP nanowires. *Nano Lett.* **12**, 5919–5923 (2012).
40. D. Dalacu, P. J. Poole, R. L. Williams, Tailoring the geometry of bottom-up nanowires: Application to high efficiency single photon sources. *Nanomaterials (Basel)* **11**, 1201 (2021).